Mesoscale Circulations Forced by Melting Snow. Part I: Basic Simulations and Dynamics

KIT K. SZETO AND CHARLES A. LIN

Department of Physics, University of Toronto, Toronto, Ontario, Canada

RONALD E. STEWART

Cloud Physics Research Division, Atmospheric Environment Service, Downsview, Ontario, Canada

(Manuscript received 20 June 1986, in final form 3 October 1987)

ABSTRACT

The melting of snow extracts latent heat of fusion from the environment. The basic response of the atmosphere to this cooling-by-melting mechanism is investigated by using a nonlinear two-dimensional numerical model. It is found that the resultant melting-induced circulations consist of a forced downdraft which spreads out laterally like a gravity current and transients which are gravity waves. The characteristics of these mesoscale thermally driven circulations are studied under idealistic atmospheric conditions. Model results show that the melting associated with realistic precipitation rates (up to 10 mm h^{-1}) can induce horizontal wind perturbations of several meters per second and vertical motions of tens of centimeters per second. Since the gravity waves and the cold outflow current propagate away from the source, they can have significant dynamic effects on the environment remote from the precipitation region. Moreover, the melting-induced, near 0°C isothermal layer in the atmosphere alters the local static stability. It is inferred that these melting-induced effects may significantly influence the momentum and moisture transports in mesoscale precipitation systems.

1. Introduction

Microphysical processes interact with atmospheric flows in many ways. A large number of studies have been conducted on the dynamic effects of the phase changes of water, especially those of condensation and evaporation (see, for example, Brown 1979; Thorpe et al. 1980). Comparatively little work has addressed the response of the atmosphere to melting.

The thermodynamic influence of melting results from the extraction of the latent heat of fusion from the atmosphere. Although the latent heat of fusion is about an order of magnitude smaller than the latent heat of sublimation or evaporation, the melting of snowflakes, unlike condensation, evaporation and freezing, is restricted to a narrow layer just below the 0°C level. The resultant cooling can result in the development of a near 0°C isothermal layer.

The melting process can influence the dynamics of the atmosphere via two different mechanisms. First, if there are horizontal variations in the precipitation rate, ambient air temperature or topography, there will be differential horizontal cooling in the melting layer. This will in turn produce horizontal gradients of pressure perturbations in the melting regions. Second, there is enhanced static stability above and through the near 0°C isothermal layer and the development of instability below it. Only a few studies have addressed these dynamic consequences.

Atlas et al. (1969) presented a detailed Doppler radar study of the mesoscale wind perturbations induced by melting snow. They found that the spatial frequency of these wind perturbations was the same as the variation in the precipitation pattern. Less specific but related observational studies can also be found in Harrold and Browning (1967), Heymsfield (1979) and Carbone (1982).

Atlas et al. (1969) tried to explain their observations by modeling a hydrostatic, nonrotating inviscid atmosphere with no vertical motion. They showed that 1 mm of melted snow would produce a 350 m deep 0°C isothermal layer and a pressure increase of 0.12 mb at the base of the layer. They then inferred that a "meso-high" would form downwind of the precipitation core region. The adjustments of the ambient wind field to the meso-high produced the observed wind perturbations. By assuming steady state conditions, they were able to obtain horizontal wind perturbations in rough agreement with observations.

Lin and Stewart (1986) studied the steady state response of the atmosphere to prescribed temperature perturbations corresponding to typical melting environments. They used a linear, two-dimensional model with the effects of friction and rotation included. Thermally driven circulations having a length scale similar

Corresponding author address: Dr. Charles Lin, Climate Research Group, Department of Meteorology, McGill University, 805 Sherbrooke Street West, Montreal, Quebec H3A 2K6 Canada.

to that of the temperature perturbations were produced. They suggested that the updraft branch of this type of circulation might cause enhanced precipitation in a saturated environment. Although there are obvious deficiencies in the two aforementioned models, at least to the authors' knowledge they are the only theoretical studies addressing the melting-induced circulation problem.

Despite the lack of theoretical understanding of the basic mechanisms involved, various authors have suggested that the dynamic effects of melting can be substantial in extratropical and deep tropical systems. Braham (1952) believed that melting is partially responsible for the downdraft of a thunderstorm, although he was not able to give a quantitative estimate of this effect. Leary and Houze (1979) reported that melting (together with evaporation) might play an important role in the initiation and maintenance of mesoscale downdrafts beneath the anvil clouds of deep tropical convection. In a case study of a warm frontal system, Heymsfield (1979) proposed that the vertical transport of horizontal momentum by melting-induced mesoscale circulations may have important effects on the large-scale dynamics. Carbone (1982) proposed that the diabatic cooling in the melting layer behind a frontal rainband is a sustaining frontogenetic mechanism in that it could establish a "resonance" with synoptic-scale cold air advection and frontal forcing. Marwitz (1983) found that melting has significant dynamic effects on the airflow and precipitation organization in certain orographic storms. Stewart (1985) and Stewart and King (1987) suggested that dynamic effects of melting may be responsible for the mesoscale organization of precipitation in a rain/snow boundary area. The ideas attributed to melting-induced dynamics in the papers cited above are mainly inferred from observational data. This is clearly an area where mesoscale observations have outrun theoretical research.

The purpose of the present study is to simulate numerically the dynamic consequences of melting. The goal is to provide a firm theoretical foundation for the observational and more complex numerical studies of mesosystems in which melting plays a role. The melting problem is studied here as a distinct fluid-dynamical problem. No attempt is made to simulate the initiation of precipitation and the coevolution of the melting-induced circulations and the precipitation system. We assume that a steady-state precipitation system has already formed at the initial time. The dynamic response of the atmosphere to the melting of the ice-phase precipitation below 0°C level is then simulated with a nonlinear, time-dependent, two-dimensional numerical model. Some of the assumptions used in the models of Atlas et al. (1969) and Lin and Stewart (1986) are relaxed and some microphysics is included.

The next section provides a description of the model. Results of basic runs are presented in section 3. Discussions and conclusions are given in sections 4 and 5.

2. Model description

a. Basic assumptions and model equations

For simplicity, we utilize a two-dimensional (2-D) model in the present study. Variations of the predicted variables in the y-direction are ignored. The 2-D mesoscale numerical model used in this study is very similar to that described by Orlanski and Ross (1977) and interested readers are referred to their paper for further details.

To isolate the dynamic effects of melting, a number of assumptions are made. Moist processes and the effects of precipitation drag are neglected. The model is assumed to have flat terrain, and no surface heat source and sink is considered. Utilizing the "deep anelastic" approximation (Ogura and Phillips 1962), the model equations formulated using the streamfunction ψ and y-component vorticity η for motion in the x–z plane are

$$\frac{\partial \eta}{\partial t} = J(\psi, \alpha_0\eta) + f\frac{\partial v}{\partial z} - \frac{g}{\theta_0}\frac{\partial \theta}{\partial x} + \frac{\partial}{\partial x}\nu_H\frac{\partial \eta}{\partial x} + \frac{\partial}{\partial z}\nu_z\frac{\partial \eta}{\partial z} \tag{2.1}$$

$$\frac{\partial v}{\partial t} = \alpha_0 J(\psi, v) - f\left(\alpha_0\frac{\partial \psi}{\partial z} - U\right) + \frac{\partial}{\partial x}\nu_H\frac{\partial v}{\partial x} + \frac{\partial}{\partial z}\nu_z\frac{\partial v}{\partial z} \tag{2.2}$$

$$\frac{\partial \theta}{\partial t} = \alpha_0 J(\psi, \theta) - v\frac{\partial \theta_g}{\partial y} + \frac{\partial}{\partial x}K_H\frac{\partial \theta}{\partial x} + \frac{\partial}{\partial z}K_z\frac{\partial \theta}{\partial z} + \frac{\theta_0 \dot{Q}}{C_p T_0} \tag{2.3}$$

$$\eta = \frac{\partial}{\partial x}\left(\alpha_0\frac{\partial \psi}{\partial x}\right) + \frac{\partial}{\partial z}\left(\alpha_0\frac{\partial \psi}{\partial z}\right) \tag{2.4}$$

$$\alpha_0\frac{\partial \psi}{\partial z} = u \tag{2.5}$$

$$-\alpha_0\frac{\partial \psi}{\partial x} = w \tag{2.6}$$

$$\frac{\partial \theta_g}{\partial y} = -\theta_g\frac{f}{g}\frac{\partial U}{\partial z} \tag{2.7}$$

$$\alpha_0 = \alpha_0(z) = \frac{1}{\rho_0} = \frac{RT_0(z)}{P_0(z)}. \tag{2.8}$$

The notation is conventional and a list of symbols is in the Appendix. The advective effects are represented in Jacobian form. The Jacobian $J(A, B)$ is defined as

$$J(A, B) = \frac{\partial A}{\partial x}\frac{\partial B}{\partial z} - \frac{\partial A}{\partial z}\frac{\partial B}{\partial x}.$$

The last term on the right-hand side of (2.3) represents the diabatic cooling effect of melting which is the forcing mechanism in this system.

b. Numerical aspects

The system of partial differential equations (2.1)–(2.4) is solved numerically by using the leapfrog (centered in time and space) finite differencing scheme. The diffusion terms are lagged by one time step and the Coriolis terms are treated implicitly for the sake of computational stability. In order to reduce truncation error, the flow variables are specified over a staggered grid throughout the field. Finite differencing of the Jacobian terms is treated using the Arakawa (1966) formulation to minimize nonlinear numerical instability. To suppress the time mode splitting associated with the leapfrog scheme, a Robert frequency filter (Asselin 1972) is applied at every time step. The finite difference analog of (2.4) is solved directly by inverting the block tridiagonal matrix of the resulting algebraic system of equations. The grid net consists of 141 evenly spaced grids in the vertical and 51 grids in the horizontal. In the simulations to be presented below, $\Delta z = 70$ m, $\Delta x = 2$ km and $\Delta t = 20$ s unless otherwise stated.

c. Parameterizations

1) SUBGRID-SCALE TURBULENCE PARAMETERIZATIONS

The lapse rate at the base of the melting-induced isothermal layer becomes superadiabatic and therefore convectively unstable. Resulting convection will affect the thermodynamics in the melting layer and may influence the larger-scale melting-induced circulations. The resolution of the present model is, however, too coarse to resolve these convective motions properly. It is therefore desirable to choose an eddy viscosity parameterization scheme that accounts for increased turbulence production in convective instability. The scheme to be used is that of Orlanski and Ross (1973) and takes the form:

$$\nu_z = K_z = \begin{cases} K_{z0}\left[1 + c\left(-\dfrac{g\Delta\theta(\Delta z)^3}{\theta K_{z0}\nu_{z0}}\right)^{1/3}\right], & \Delta\theta < 0 \\ K_{z0}, & \Delta\theta \geq 0 \end{cases} \tag{2.9}$$

where K_{z0} and ν_{z0} are the constant background values of vertical eddy diffusivity and viscosity, respectively; Δz and $\Delta\theta$ are local values of the vertical grid-spacing and vertical potential temperature difference across the grid box, respectively; and c is a constant, preset as 0.1 in the following simulations. This single scheme will be applied to the whole model domain. Horizontal diffusion is included in the model to provide additional numerical smoothing. The horizontal exchange coefficients are assumed to be related to the vertical values by

$$K_H = D\left(\frac{\Delta x}{\Delta z}\right)^2 K_z \tag{2.10}$$

where D is a constant set at 5.0 in this study. The K_{z0} is set at 0.3 m^2 s^{-1} in the following experiments.

2) PARAMETERIZATION OF COOLING BY MELTING

The treatment of the melting microphysics in the model is a generalization of the 1-D scheme of Matsuo and Sasyo (1981a). As a first attempt, microphysical processes such as aggregation, riming, breakup, etc., are neglected. Moreover, the water vapor density in the ambient air is assumed to be equal to the saturated vapor density at the melting particle surface (at 0°C), so that neither evaporation/sublimation nor condensation will affect the melting of the particles. Only snow particles are considered in this study, although the inclusion of hail and graupel particles in the present scheme is rather straightforward.

A two-dimensional stationary precipitation pattern is prescribed at the initial 0°C level in the x–z plane. The precipitation region is assumed to have infinite extent in the y-direction. The horizontal variation of precipitation rate at the 0°C level is prescribed as an initial condition and is assumed to be invariant with time. The precipitation field is then discretized as parcels of snow particles contained in a unit mass of air at the 0°C level grid points. One parcel is released at a 0°C level grid point within the precipitation pattern at the beginning of each time step. Assuming that all the snow particles are spherical and of the same size, the number of particles N_i in the ith parcel can be calculated from the precipitation rate $R(x)$ at the grid point where the parcel originated.

Each precipitation parcel is assumed to move with a velocity equal to that of the air plus the particles' terminal velocity. Since the terminal velocity of the particles varies as they melt, the number of particles in each parcel is updated at each time step to ensure that this number is equal to the number of particles that will be contained in a unit mass of air. A snow particle is defined as totally melted when its size reaches that of the raindrop of equivalent mass.

The melting rates of the snow particles are calculated from the equation

$$L_f\frac{dm}{dt} = -2\pi r k_a \,\mathrm{Nu}(T_a - T_s). \tag{2.11}$$

Here, L_f is the latent heat of fusion of ice and is assumed to have a constant value of 333 700.0 J kg^{-1}. The m and r in (2.11) are the mass and radius of a melting particle, and T_a and T_s are the ambient air temperature and the particle surface temperature (0°C). This equa-

tion states that the latent heat absorbed by a melting particle is equal to the sensible heat loss by the ambient air. The formulation of the Nusselt number Nu is adapted from Matsuo and Sasyo (1981a):

$$\mathrm{Nu} = 3.50(1.0 + 0.275\ \mathrm{Pr}^{0.33}\ \mathrm{Re}^{0.5}). \quad (2.12)$$

The terminal velocity V_T of the particles is calculated from the equation:

$$V_T = (4Dg\rho_i/3C_D\rho_a)^{1/2} \quad (2.13)$$

where D is the diameter of a particle, C_D is the particle drag coefficient and ρ_i and ρ_a are the densities of the particle and of the air, respectively. The melted water is assumed to be trapped inside the particle, as supported by the observations of Knight (1979). As a consequence, the density of a particle is allowed to vary from the unmelted value to a value approaching that of a raindrop. The drag coefficient of a particle is assumed to vary linearly from an initial unmelted value of 1.2 to the drag coefficient C_{DR} of the equivalent mass raindrop as given by

$$C_D = 1.2 - (1.2 - C_{DR})(D_0 - D)/(D_0 - D_R). \quad (2.14)$$

Here, D_0 denotes the unmelted particle diameter and D_R is the equivalent mass raindrop diameter. Applying (2.13) to a raindrop gives the raindrop surface drag coefficient as

$$C_{DR} = \frac{4g}{3\rho_a}\rho_w D_R V_{TR}^{-2}. \quad (2.15)$$

The terminal velocity of raindrops was determined empirically by Best (1950) as

$$V_{TR} = 9.32\{1.0 - \exp[-(D_R/1.77)^{1.147}]\} \quad (2.16)$$

where D_R is in mm and V_{TR} is in m s^{-1}.

The cooling rate of the air at the location of the ith precipitation parcel is calculated from

$$\dot{Q}_i = N_i L_f \left(\frac{dm}{dt}\right)_i \quad (2.17)$$

where $(dm/dt)_i$ is calculated from (2.11). These cooling rates are then analyzed objectively back to each grid point via a distance-weighted averaging procedure. The $\dot{Q}(I, J)$ at each grid point (I, J) is then multiplied by a constant equal to $\Sigma\ \dot{Q}_i/\Sigma\ \dot{Q}(I, J)$ so that the total cooling at the grids is consistent with that associated with the parcels.

d. Boundary conditions

The radiation conditions developed by Orlanski (1976) are employed to simulate open lateral boundaries. A free-slip rigid lid with lapse rate fixed at the initial value is assumed at the top. A spongy layer is applied to the upper layers to absorb any vertically propagating gravity waves. The lower boundary is rigid, free-slip and adiabatic.

3. Results

Results for the basic runs will be presented in this section. The simulations are initialized with a geostrophic and hydrostatic basic state. No initial horizontal temperature gradient is assumed. The precipitation pattern is assumed to have a Gaussian variation of precipitation rate in the horizontal:

$$R(x) = R_m \exp[-(X - X_m)^2/(a\Delta x^2)] \quad (3.1)$$

where $R(x)$ is the precipitation rate at the initial melting level, R_m is the maximum precipitation rate, and a is the spatial rate constant. In the results presented here, $R_m = 10$ mm h^{-1} and $a = 12$. The radius and density of the snow particles are set to be 4 mm and 25 kg m^{-3}. The precipitation pattern used here may, for example, represent a rainband in an extratropical cyclone. Initial temperature conditions used are typical autumn conditions in the midlatitudes:

$$\frac{\partial\theta_0}{\partial z} = \begin{cases} 1\ \mathrm{K\ km^{-1}}, & z < 980\ \mathrm{m} \\ 2\ \mathrm{K\ km^{-1}}, & 980 \leqslant z < 2800\ \mathrm{m} \\ 4\ \mathrm{K\ km^{-1}}, & z \geqslant 2800\ \mathrm{m} \end{cases}$$

with a surface temperature of 10°C.

a. Rest basic state runs

1) THE REFERENCE RUN

No basic state wind is assumed in this control experiment. The Gaussian precipitation pattern is centered at the middle of the domain and distributed over 17 grid locations in the horizontal. With the lapse rates and surface temperature as defined above, the initial 0°C level is located at $z = 1.26$ km.

The response of the model atmosphere to the melting consists of two major circulation cells with an axis of symmetry through the core of the precipitation. There is a forced downdraft at the precipitation core, chilled outflows below the melting layer, updrafts at the outer branches of the cells, and return flows at and above the melting layer to close the circulations. Figures 1a–c show the evolution of the perturbation streamfunction ψ' with time. An interesting time-dependent behavior of these circulation cells is that their aspect ratio decreases with time. This behavior results from the lateral propagation of the outer flanks of the cells. The circulation cores also propagate away from the source region, but at slower speeds than those associated with the outer flanks. In the mature stage (Fig. 1c), the outflow looks similar to that of a gravity current with a well-defined "head" structure.

Figure 2 shows the x-velocity field at $t = 67.0$ min and $t = 100.0$ min. The most noticeable feature of these results is the strong shear at the base of the melting layer. The maximum magnitude of u reaches a steady value of $\approx$9 m s^{-1} by about 1 h. In the real atmosphere,

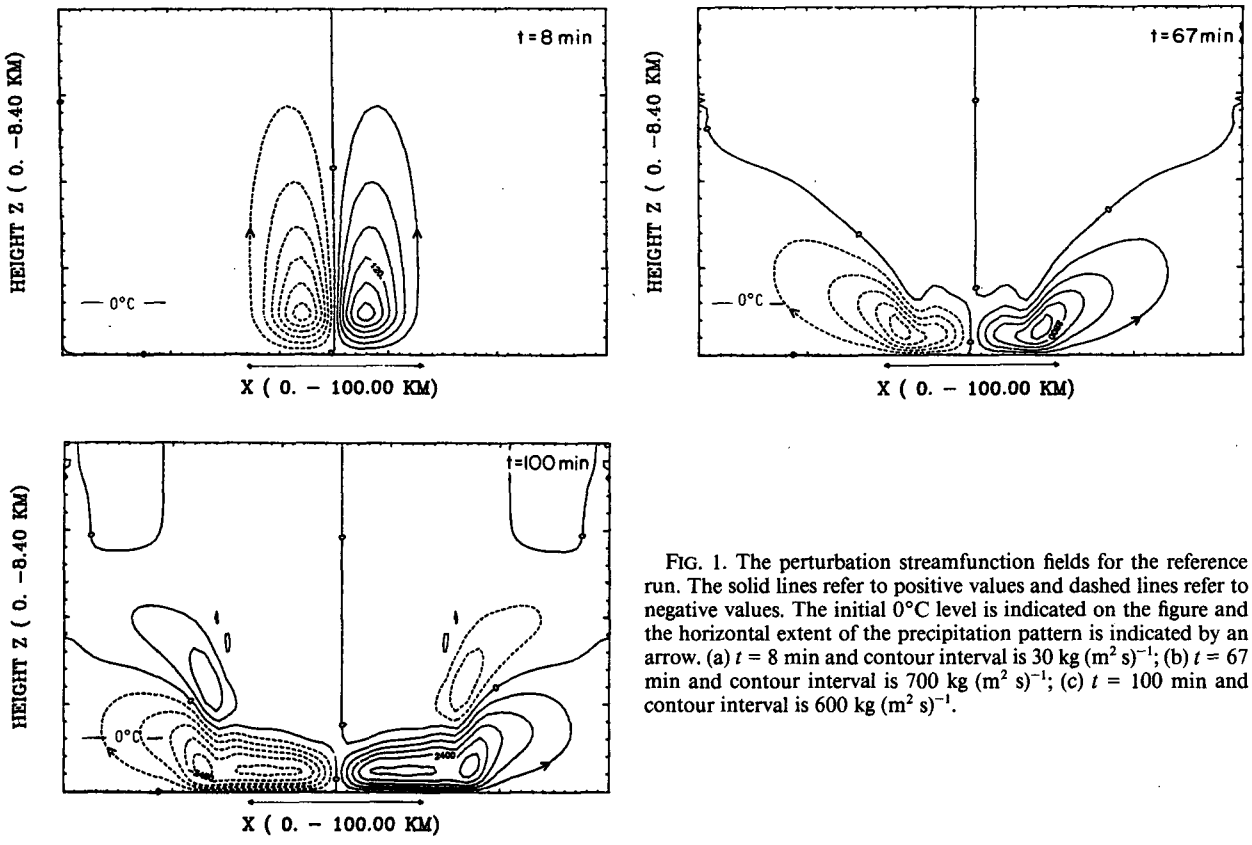

FIG. 1. The perturbation streamfunction fields for the reference run. The solid lines refer to positive values and dashed lines refer to negative values. The initial 0°C level is indicated on the figure and the horizontal extent of the precipitation pattern is indicated by an arrow. (a) t = 8 min and contour interval is 30 kg $(m^2\ s)^{-1}$; (b) t = 67 min and contour interval is 700 kg $(m^2\ s)^{-1}$; (c) t = 100 min and contour interval is 600 kg $(m^2\ s)^{-1}$.

we may expect the region of maximum perturbation horizontal velocities to be more confined to the melting layer due to surface stress. At the mature stage, sharp horizontal gradients in u exist at the "head" regions of the outflow. The y-velocity field (not shown here) is similar to the u field but with the signs reversed. This change in sign between u and v is due to the Coriolis effect which causes a veering of the resultant velocities with time. The maximum magnitude of v reaches 2.0 m s^{-1} by the end of the integration (t = 100 min).

Figure 3 shows the vertical velocities at 67.0 min. The strongest downdraft does not occur at the precipitation core but rather at regions above and to the rear of the outflow-current heads. The strongest updraft occurs at the regions immediately ahead of the outflow-current heads where intense horizontal convergence takes place. The maximum magnitudes of the induced downdraft and updraft are about 70.0 and 45.0 cm s^{-1}, respectively. Figure 3 also illustrates that internal gravity waves are generated when the model atmosphere responds to the chilling from the melting snow.

Figure 4 shows a portion of the temperature profile and vertical distribution of $\dot{Q}$ at times t = 33.0, 67.0 and 100.0 min and at x = 56.0 km. The precipitation rate through the melting level at this location is about 5.0 mm h^{-1}. A 400 m deep isothermal layer at $\approx$1°C is formed by about 33 min. The reasons for the production of an isothermal layer warmer than 0°C will be discussed later. The lapse rate beneath this isothermal layer is unstable. The turbulence parameterization scheme is activated in this unstable region and restores the stable conditions by later times. Since these convective mixing processes raise the temperatures in the melting layer, they have a positive feedback effect on the melting (cooling) rates (Fig. 4).

Figures 5a–c show the temporal evolution of the perturbation potential temperature field. Because the initial cooling is confined to the region directly affected by melting, diabatic cooling is the dominant factor in determining the thermodynamical structure at the early stage of the disturbance. Later, the melting-chilled air is advected out of the precipitating region as the perturbation horizontal velocities develop. At the same time, melting maintains the supply of cool air in the source region. Adiabatic warming and cooling are also associated with the vertical motions. As a consequence, the temperature of the melting-induced isothermal layer is warmer than 0°C (as might be expected from the consideration of melting alone). The melting-chilled air is mainly confined to the precipitation region in the first hour. After the first hour, the cool air sinks to the surface and starts spreading out horizontally. These

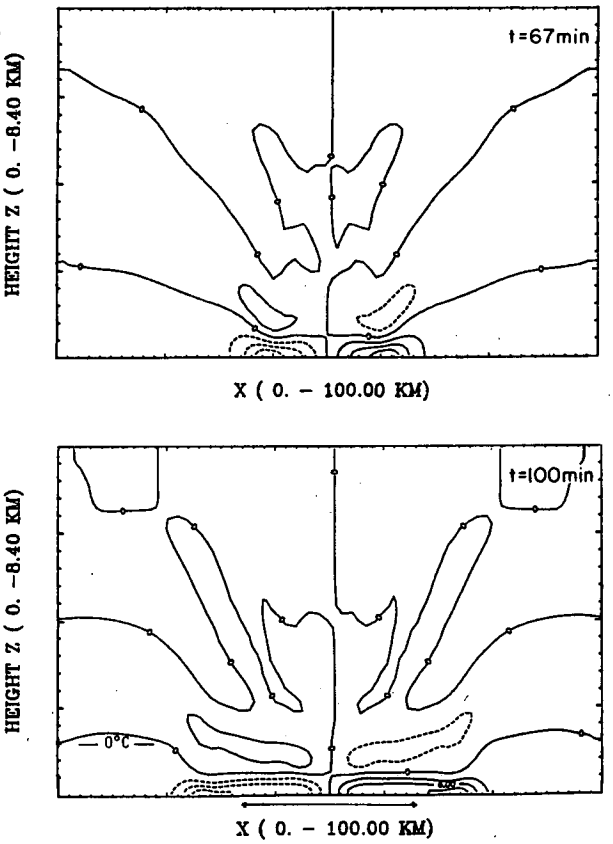

FIG. 2. As in Fig. 1 except for the perturbation x-velocity field at t = 67 min and 100 min, respectively. Contour interval is 3 m s^{-1}.

figures also indicate that sharp horizontal temperature gradients exist at the "fronts" of the outflow currents.

Figures 6a and b show the temporal variation of the maximum magnitudes of ψ' and w', respectively. The growth rate of the disturbance remains constant for the first hour and then tapers off. The maximum updraft at the front of the outflow current reaches a nearly constant value of about 0.45 m s^{-1} by 1 h. This indicates that the horizontal convergence at the front and the speed of the front itself reach a nearly constant value after the first hour.

2) SENSITIVITY EXPERIMENTS

Several sensitivity experiments have been performed with the rest basic state simulations. The results of these studies are summarized briefly in this section.

(i) *Changing the precipitation rate.* The precipitation rate can be changed by varying the maximum precipitation rate, R_m, or by changing the spatial rate constant, a, in (3.1). Increasing R_m implies increasing both the magnitude of the cooling rate and the horizontal gradient of the cooling. With R_m doubled to 20.0 mm h^{-1}, the magnitudes of both the maximum horizontal and vertical velocities were increased by a factor of $\sim$1.3 when compared to the reference case. An outflow current is also established sooner than in the control run.

Increasing the spatial rate constant with R_m kept constant gives a more stratiform precipitation field. The thermally induced circulations become more concentrated at the edges of the precipitation pattern in such cases. The downdraft at the position of the precipitation becomes more widespread and the magnitudes decrease as compared to the reference case.

(ii) *Altering the basic temperature field.* The basic temperature field can be changed by altering either the initial lapse rates or the surface temperature. Decreasing the static stability increases the height of the thermal circulations and decreases the width. For a situation with neutral stratification in the lowest 3 km, the vertical velocities increase threefold and the maximum horizontal velocities increase by a factor of $\sim$1.5 over the reference run. If the static stability is increased, the intensities of the thermal circulations decrease and the circulations are confined more to the vicinity of the freezing level. In situations with a strong surface inversion, the downdraft remains above the inversion throughout the integration.

With a higher 0°C level, the resulting circulations are elevated from the surface (Figs. 7a and 7b). The forced downdraft at the source region remains above the surface throughout the integration. As a result, the outflow speeds are lower than that in the reference case and the flow structure no longer closely resembles a gravity current. The disturbance also grows at a slower rate than in the control case.

(iii) *Changing other parameters.* The thermal circulations are qualitatively unchanged for a variation in the background eddy viscosity values. However, if the eddy parameterization scheme is deactivated, convective motions having depths of a few hundred meters

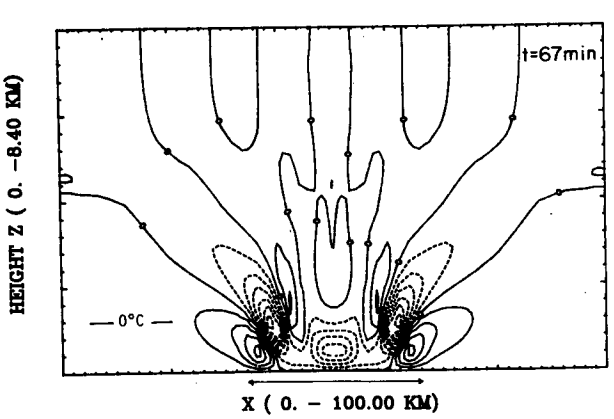

FIG. 3. As in Fig. 1 except for perturbation z-velocity field at t = 67 min. Contour interval is 10 cm s^{-1}.

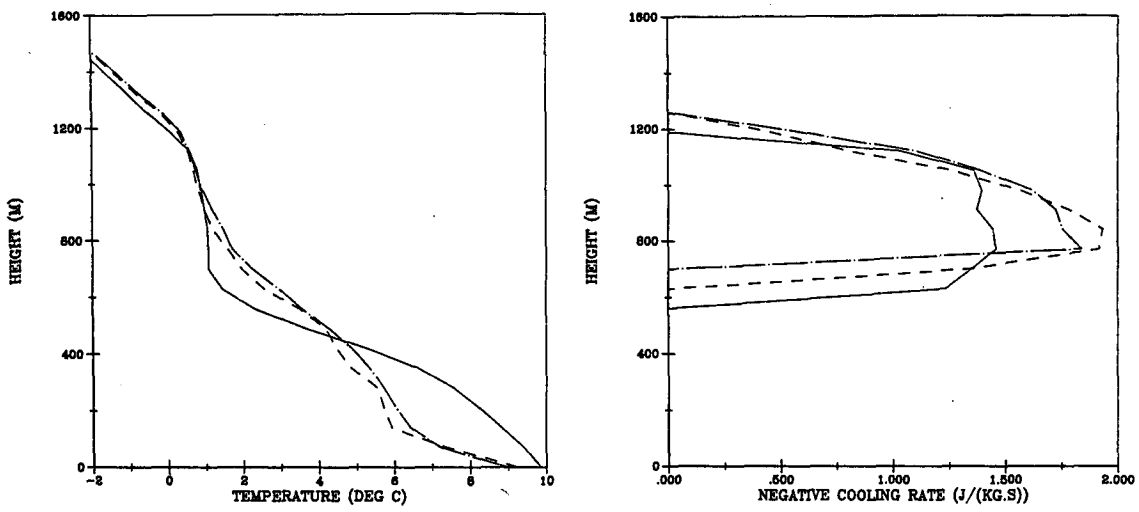

FIG. 4. Portion of the vertical temperature profile and vertical distribution of $\dot{Q}$ at $x = 56$ km for the reference run. Solid line: $t = 33$ min; dashed: $t = 67$ min; dash-dot: $t = 100$ min.

are induced at the base of the isothermal layer. The resolution of the present model is insufficient to handle these small eddies properly, which eventually gives rise to numerical instabilities. These small-scale convective motions may correspond to the small-scale wind perturbations that Harrold and Browning (1967) and Atlas et al. (1969) observed beneath the 0°C layer.

Decreasing the size of the snow particles accelerates their melting and results in a faster growth rate for the circulations. Increasing the densities of the snow par-

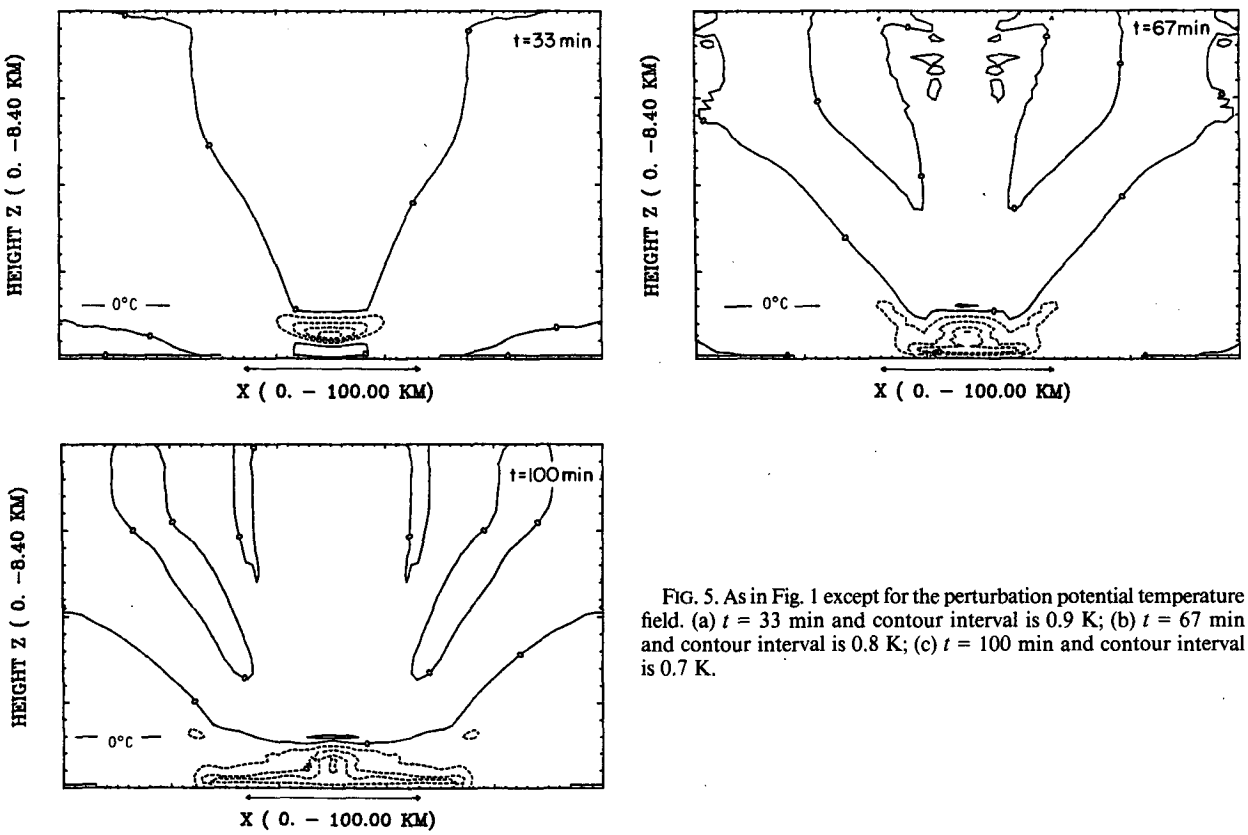

FIG. 5. As in Fig. 1 except for the perturbation potential temperature field. (a) $t = 33$ min and contour interval is 0.9 K; (b) $t = 67$ min and contour interval is 0.8 K; (c) $t = 100$ min and contour interval is 0.7 K.

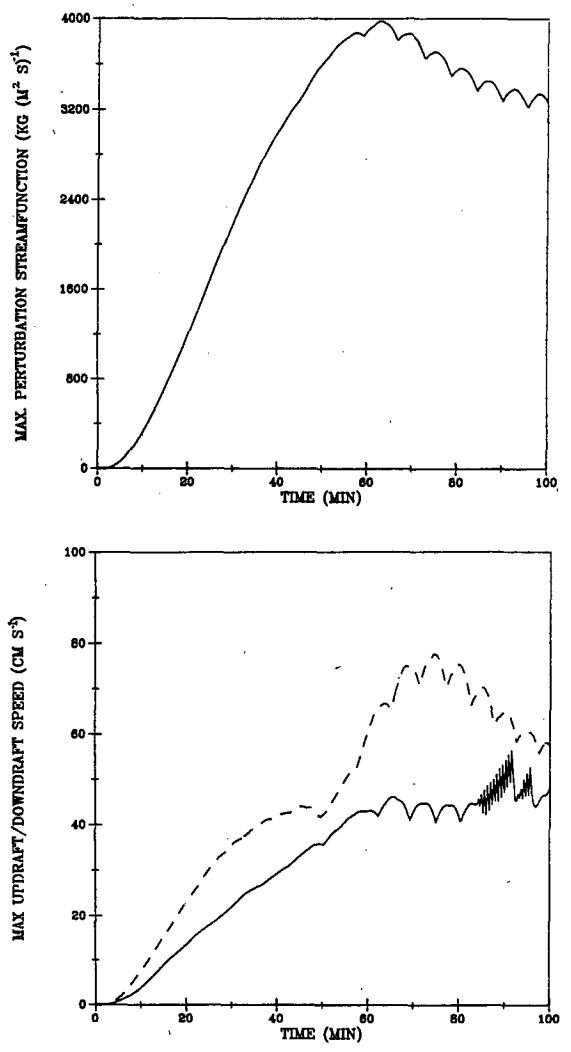

FIG. 6. (a) The variation of maximum perturbation streamfunction magnitude with time for the reference run. (b) As in (a) except for the maximum updraft and downdraft magnitudes (solid: updraft, dashed: downdraft).

ticles implies increasing the corresponding terminal velocities. This increases the thickness of the melting layer but decreases the values of the cooling rate Q. With the particle density increased to 500.0 kg m^{-3} (this is more likely a graupel-melting case), both the chilled air and the thermal circulation are closer to the surface than in the reference case. The overall intensities of the circulations are weaker than those in the control case.

b. *The mean flow run*

In this simulation, a mean wind $U(z)$ is introduced. For the sake of simplicity, the vertical wind shear is assumed to be confined to the planetary boundary layer ($\sim$1 km deep) only. Here U is assumed to decrease linearly from 15 m s^{-1} at the surface to 0 m s^{-1} at the 0°C level (at z = 1.26 km). Above the 0°C level, the mean wind is assumed to be zero so that the precipitation pattern is stationary in the model domain. The location of the maximum precipitation is at x = 34 km. All other parameters are the same as in the reference case.

Figures 8a–c show the temporal evolution of the perturbation flow field. In the initial growth stage, there is no major difference between the results here and the rest basic state run. The flow structure for the two cases differs markedly after the initial stage. Due to the effects of the mean flow, the downwind cold outflow current speed is enhanced while the outflow at the upwind direction is retarded (Fig. 9). At the mature stage, the horizontal potential temperature gradient is greater in the upwind direction than in the downwind direction. As a consequence, the upwind circulation cell is more intense than the downwind one. Moreover, the upwind cell is located at more or less the same position throughout the integration while the downwind cell moves constantly out of the model domain. As a result,

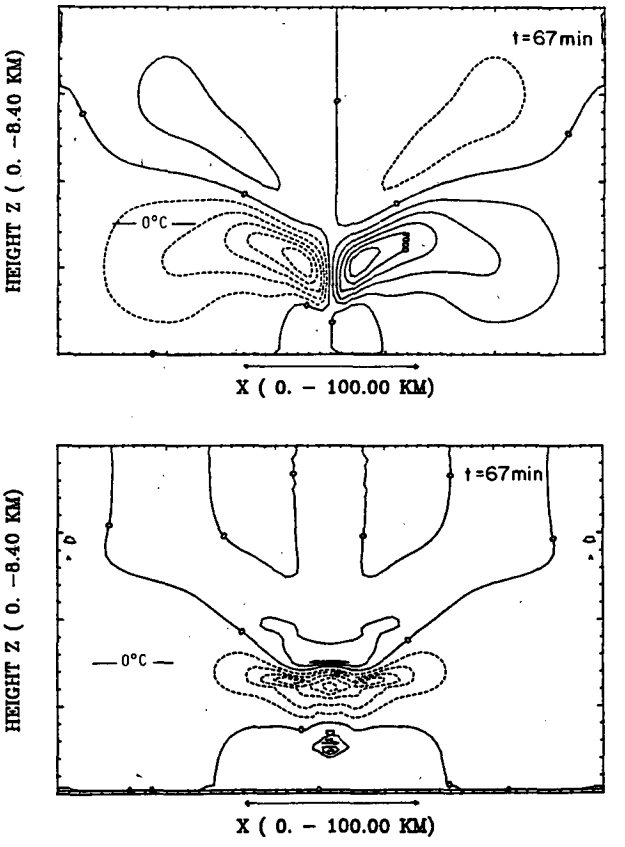

FIG. 7. (a) The perturbation streamfunction field as in Fig. 1 except for a run with surface temperature increased to 25°C (t = 67 min). Contour interval is 500 kg (m^2 s)$^{-1}$. (b) As in (a) except for perturbation potential temperature. Contour interval is 0.4 K.

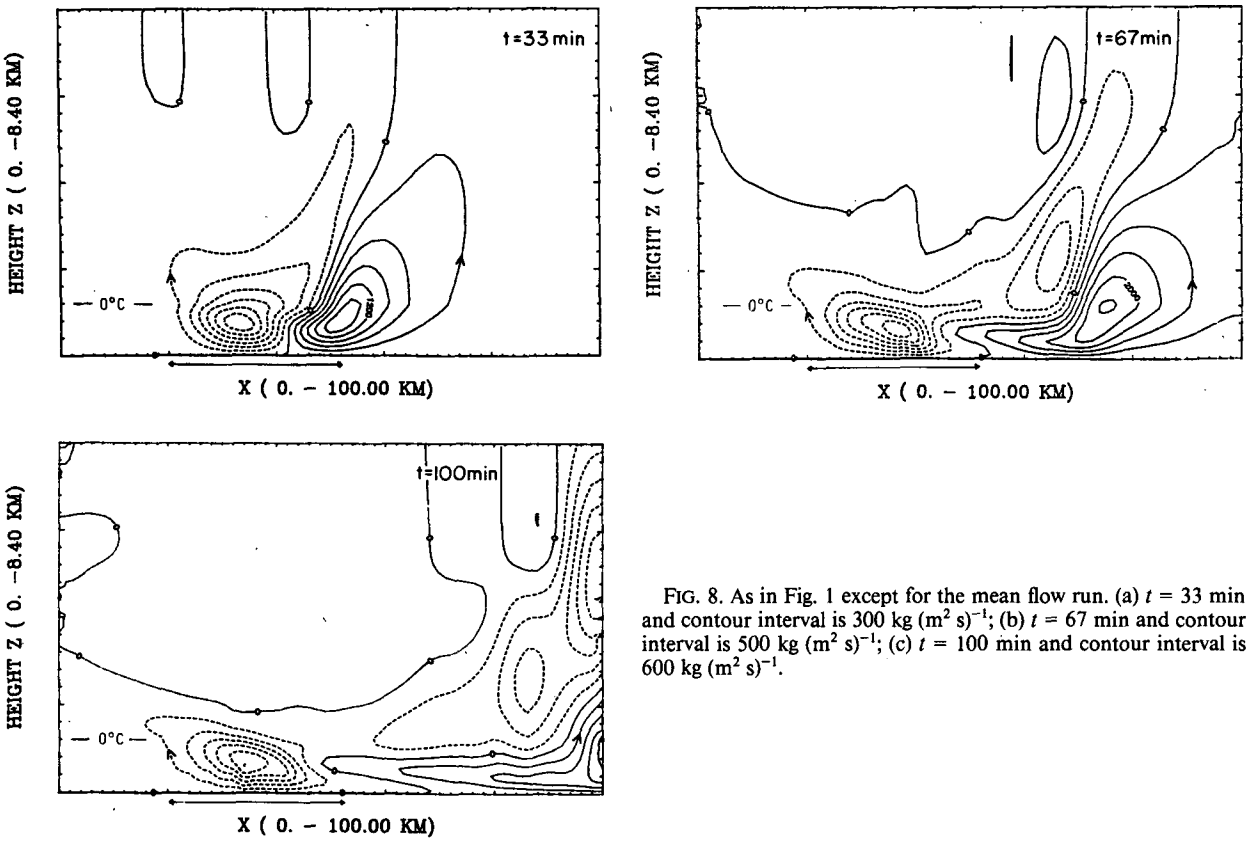

FIG. 8. As in Fig. 1 except for the mean flow run. (a) t = 33 min and contour interval is 300 kg $(m^2\ s)^{-1}$; (b) t = 67 min and contour interval is 500 kg $(m^2\ s)^{-1}$; (c) t = 100 min and contour interval is 600 kg $(m^2\ s)^{-1}$.

the strongest updraft occurs at the precipitation region throughout the integration. The results also show large amplitude gravity waves above and to the rear of the downwind cell. The maximum perturbation velocities reach −8.0 and 5.0 m s^{-1} for u and −0.5 and 0.3 m s^{-1} for w.

A 400 m deep near 0°C isothermal layer is formed inside the precipitation region. Model results also show that a 3°C isothermal layer is formed downwind of the precipitation region (Fig. 10). Apparently, this isothermal layer is formed by the downstream advection of the melting-chilled air at the precipitation region.

4. Discussion

Diagnosis of the model results enables us to give a qualitative description of the dynamics involved in melting-induced circulations. When melting commences at t = 0, the air in the vicinity of the melting level is chilled. This causes a positive pressure perturbation and accelerating outflows beneath the melting layer. In the initial stage, there is no perturbation of potential temperature above the melting layer. Consequently, the vertical variation of the (hydrostatic) pressure-gradient force will be zero away from the melting layer and the return flow will take place uniformly above it. This is why the initial circulation has large vertical extent.

If the mean stratification is stable, gravity waves will be excited by the vertical motions at the source region. For the rest basic state cases, there is a symmetry in the amplitudes of the left and right propagating waves. Results from a linear model of the melting problem (Szeto 1986) show that the amplitudes of the gravity wave modes increase with their phase speeds. The superposition of the effects of the gravity waves determines the perturbation velocity and temperature field outside the source region. These wind and temperature perturbations are local effects and are not caused by the advection of the cold air from the source region. The vertical velocities associated with these wave motions cause a redistribution of potential temperature which tends to concentrate the return flow near the melting level. Since these waves propagate constantly away from the source region, the horizontal extent of the circulation increases indefinitely with time (see Figs. 1a–c).

If the mean stratification is nearly neutral or unstable, the gravity waves will be weak or absent. The temporal behavior of the circulation then depends more on the nonlinear advection of cold air out of the precipitating region. However, the nonlinear overturning

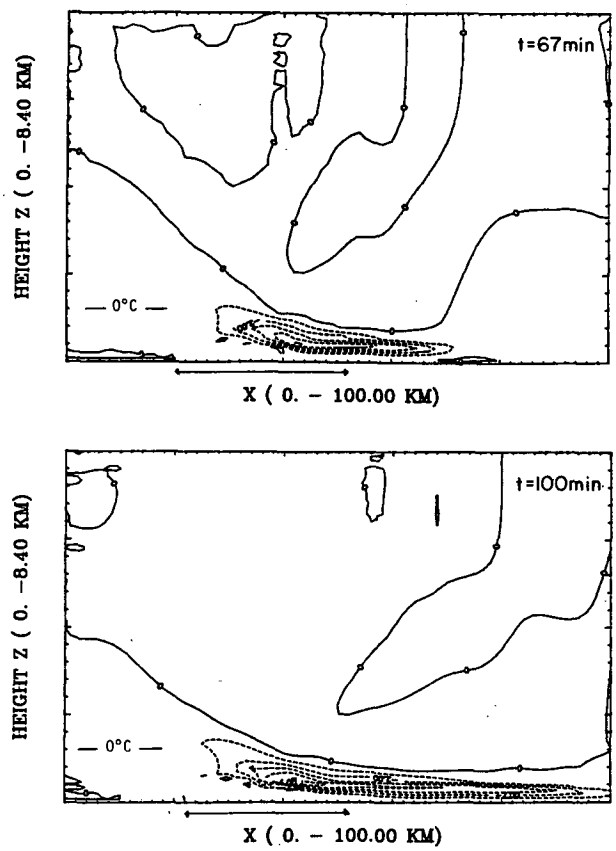

FIG. 9. Perturbation potential temperature fields at t = 67 (top) min and t = 100 min (bottom) for the mean flow run. Contour interval is 1.0 K.

propagates away from the source region at a rate substantially slower than that associated with the gravity waves. Thus the horizontal scale of the circulations is confined more to the precipitating region in a neutral or unstable environment.

If a mean flow is present, then the frequencies of the gravity waves are Doppler shifted. Linear theory (Szeto 1986) shows that the upstream propagating waves would have larger amplitudes than the downstream propagating waves and that the wave amplitudes would increase with the mean wind speed U. However, if U is greater than the maximum phase speed of these waves, the wave amplitudes would decrease with U. These effects are observed in the numerical results.

A consequence of these gravity waves is that energy is transported away from the source region. This may result in the reduction of temperature perturbation magnitudes at the source region and a decrease in the strength of the main nonlinear overturning. The nonlinear overturning process is discussed in the following section.

The diabatic cooling effects of melting produce a pool of cool air which is denser than its environment. The dense melting-chilled air will sink to the equilibrium (neutral buoyancy) level. At the same time, the dense cool air may spread horizontally and act as a cold intrusion into the ambient air. This cold outflow is associated with the nonlinear advective effects of the perturbation horizontal velocities. Dynamically, the outflow current is driven by a horizonal pressure gradient acting across the lateral interface (the front) separating the two fluids. The pressure gradient exists because the hydrostatic pressure inside the denser fluid is greater than that in the less dense fluid. The cold intrusion just described is analogous to a gravity current in a homogeneous fluid.

Model results show that the cold outflow current described above is not established until a later stage of the simulation when the cold air sinks to the surface or the equilibrium level. After the establishment of the outflow current, the melting-induced circulation reaches a quasi-steady state (perturbation velocities at the source region attain nearly constant values) except at the front of the current which continues to propagate away from the precipitation area. If the precipitation system is long-lived, we may expect the advance of the outflow current to be stalled by the Coriolis effect. In such cases, we may find the melting-induced horizontal jets become more parallel to the precipitation band. The onset time for the outflow current depends mainly on the amount of cooling and the location of current (on the surface or aloft). Model results show that the surface currents have higher outflow current speeds. Moreover, a "front" (where sharp horizontal gradients in temperature and velocity exist) would be more well defined in a surface current than in an elevated current (see Figs. 5a–c and Fig. 7b). The dynamic and geometric details of the outflow current front may not be

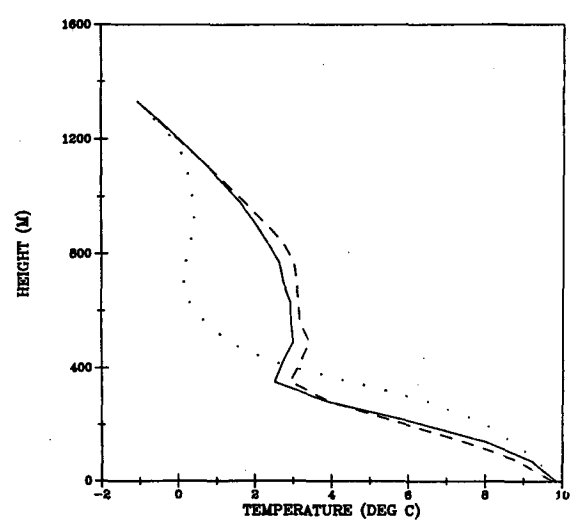

FIG. 10. Vertical temperature profiles at t = 100 min for the mean flow run. Dotted line: x = 40 km; solid line: x = 50 km; dashed line: x = 56 km.

well represented by the present model because a horizontal length scale of a few hundred meters is needed to resolve these features properly.

Model results show smaller scale wind perturbations embedded in the cold outflow current. We have mentioned that convective motions are induced at the bottom of the near 0°C isothermal layer. Since strong vertical wind shears are induced inside the melting layer, we may anticipate that Kelvin–Helmholtz waves will also be present. However, the grid size used in the present simulations may be too coarse to resolve these waves. Dynamically, these embedded smaller scale eddies will produce internal drag effects on the motion of the outflow current. These smaller scale motions may also modulate the local cloud and precipitation formation. Findeisen (1940) speculated that the convective activity at the base of the 0°C isothermal layer is responsible for the frequently observed formation of fractocumulus clouds below the rain cloud proper.

In a frame of reference moving with the front of the outflow current, we would observe an ambient wind flow over the stationary dome of dense melting-chilled air. If the stratification is stable, stationary gravity waves would be formed above and downwind of the current head (Figs. 1c, 8b and 8c). The formation of these waves is analogous to the formation of vertically propagating standing waves when a strong wind flows over a mountain in a stable environment. The vertical motions associated with these waves have magnitudes comparable to the forced downdrafts in the precipitation region.

When a mean flow (relative to the precipitation area) is present, the downstream outflow speed will be enhanced while the upstream current will be retarded. If the mean wind is strong, the upstream current may become quasi-stationary or even slowly retreat, resulting in the development of updrafts inside the precipitation region. Moreover, the horizontal convergence, and thus the updraft, at the upstream front would be much stronger than that at the downstream front. Since the upstream current is quasi-stationary, the zero wind level is a critical level for the quasi-stationary gravity waves formed above and downwind of the current head. In the results presented in section 3b, the zero wind level is located at the height of the initial 0°C level. This critical level limits the vertical propagation of these quasi-stationary gravity waves. As a result, these waves are not observed above and downwind of the upstream cell. On the contrary, large amplitude gravity waves are formed to the rear of the downstream current (Figs. 8b and 8c).

The above discussions indicate similarities between the melting-induced circulations and the sea/land breeze. The sea-breeze circulation consists of two main responses: the sea-breeze proper (the nonlinear overturning) and the sea-breeze forerunner, a series of internal gravity waves that travel inland before the arrival of the sea-breeze front (Geisler and Bretherton 1969). These responses are analogous to the cold outflow and the transient waves that we have discussed. In the well-developed stage, both circulations are characterized by two horizontal length scales: the scale of the circulation cell and the scale of the front of the outflow current.

Finally, it is worthwhile to comment on the thermodynamics of melting in light of the model results. The near 0°C isothermal layers formed in the simulations have a typical depth of 300–400 m and usually reach a quasi-steady value during the integration. These isothermal layers are somewhat shallower than the ones calculated by pure energy balance considerations (e.g., Atlas et al. 1969; Pace 1980). For example, with a precipitation rate of 4.0 mm h^{-1} and a basic lapse rate of 8.2°C km^{-1}, energy balance considerations alone would yield a 570.0 m 0°C isothermal layer in 1 h. The shallower isothermal layers obtained in the present model results are due to the combined effects of horizontal advection out of the source region, diffusion, adiabatic warming, and convective adjustments at the bottom of the isothermal layers. Results of the present model appear to agree better with observations because deep 0°C isothermal layers are rarely observed (Stewart et al. 1984). We believe that other processes in addition to melting are essential in the formations of deep ($\sim$1 km) 0°C isothermal layers, as observed by Stewart (1984). (An in-depth study of this subject will be given in Part II of this paper, Szeto et al. 1988.) The above discussion indicates that dynamic effects must be considered when studying numerically the thermodynamics and microphysics in the region of the melting layer.

5. Concluding remarks

A nonlinear 2-D numerical model has been used to study melting-induced mesoscale circulations. The response of the model atmosphere to the cooling-by-melting mechanism has been examined under idealized conditions. It has been found that the melting-induced circulations consist essentially of a forced response resembling a gravity current and transients which are internal gravity waves. The gravity current is driven by the density contrast between the melting-chilled air and the ambient air. Embedded in the gravity current are smaller-scale motions originating from convective instability. Influences of melting expand beyond the precipitation region due to the combined effects of the advance of the gravity current and the horizontal propagation of the gravity waves. With precipitation rates of up to 10 mm h^{-1}, typical perturbation velocities are of the order of a few tens of centimeters per second for w' and a few meters per second for u'.

The coupling between the dynamic effects of melting and the precipitation system and other dynamic forcings has not been considered in the present model. Moreover, neglecting condensation/evaporation may have significant effects on the calculation of the melting

rates (Matsuo and Sasyo 1981b). These idealizations make the comparison of model results with observations difficult, but they are necessary simplifications if we want to isolate the dynamic effects of melting successfully. Since most mesosystems are characteristically three-dimensional, the two-dimensional assumption is perhaps the more severe limitation of the present model.

Model results have suggested that the dynamic effects of melting can be significant enough to alter the momentum and moisture transports in storms of different scales and nature. Since the melting-induced circulations propagate away from the source region, they may have a dynamic effect on the environment remote from the precipitation source. For example, the melting-induced cold outflow at the stratiform region behind a squall line may propagate towards the leading convective elements and may eventually join and strengthen the main downdraft. We have seen that significant updraft is induced at the front of the outflow current. These updraft motions may be a significant feeding or generating mechanism for rainbands embedded in midlatitude cyclones. Locally, the melting-induced near 0°C isothermal layers enhance the static stability. These stable regions may inhibit the vertical motions in the basic wind field. On the other hand, a strong vertical shear can be supported in these isothermal layers due to the enhanced stability. As suggested by Carbone (1982), these regions may provide a favorable level for separating the inflows and outflows in frontal-convective systems. The above inferences must eventually be verified in real observations and in carefully controlled numerical experiments using more complicated models.

Future studies in this area should explore the coupling of melting-induced dynamics to the parent storms. Some possibilities are the study of: (i) the melting dynamic effects on severe convective systems; (ii) the frontogenetic/frontolytic effects of melting; (iii) the role of melting in the mesoscale precipitation organization of synoptic scale systems; and (iv) the influence of the melting dynamics in some hazardous weather events (e.g., freezing rain). Results of the present model may be used as a diagnostic tool in interpreting the outcomes of these more complicated models.

In summary, this paper has investigated the basic response of the atmosphere to the diabatic effects of melting snow. It has been shown that the coupling between the microphysical process of melting and dynamics is a complicated one, and this coupling can be significant. The melting problem is an area of mesoscale dynamics with important applications, some of which will be addressed in Part II of this paper.

Acknowledgments. This work is supported by the Atmospheric Environment Service, the Natural Science and Engineering Research Council and the University of Toronto. The authors wish to thank Ms. Ana Sousa for secretarial assistance in the preparation of the manuscript. The authors also wish to thank the three anonymous reviewers whose comments significantly enhanced the organization and clarity of the presentation.

APPENDIX

List of Symbols

The symbols not included here are defined in the text. Variables with a subscript 0 are reference state variables and primed variables are perturbations.

a	spatial rate constant in Gaussian precipitation rate
C_D	drag coefficients of snow particles
C_p	heat capacity of air at constant pressure
D	diameter of a snow particle
f	Coriolis parameter
g	acceleration due to gravity
I	horizontal grid index
J	vertical grid index
k_a	thermal conductivity of air
K_H	horizontal eddy diffusivity of heat
K_V	vertical eddy diffusivity of heat
L_f	latent heat of fusion
m	mass of a snow particle
Nu	Nusselt number
p	pressure
Pr	Prandtl number
$\dot{Q}$	cooling rate
r	radius of a snow particle
R	gas constant of dry air
Re	Reynolds number
R_m	maximum precipitation rate
$R(x)$	precipitation rate
t	time
T, Ta	air temperature
Δt	time step
u	x-velocity
$U(z)$	geostrophic basic x-velocity
v	y-velocity
V_T	terminal velocity of particles
V_{TR}	terminal velocity of raindrop
w	vertical velocity
x	horizontal distance normal to precipitation band
X_m	x-location of maximum precipitation
Δx	horizontal grid spacing
y	horizontal distance parallel to precipitation band
z	height
α	specific volume of dry air
η	y-component vorticity
ν_H	horizontal eddy diffusivity of momentum
ν_V	vertical eddy diffusivity of momentum

ρ, ρ_a density of dry air
ρ_i density of a snow particle
ψ streamfunction
θ potential temperature

REFERENCES

Arakawa, A., 1966: Computational design for long-term numerical integration of the equations of fluid motion: Two-dimensional incompressible flow, Part I. *J. Comput. Phys.*, **1,** 119–143.

Asselin, R., 1972: Frequency filter for time integrations. *Mon. Wea. Rev.*, **100,** 487–790.

Atlas, D., R. Tatehira, R. C. Srivastava, W. Marker and R. E. Carbone, 1969: Precipitation-induced mesoscale wind perturbations in the melting layer. *Quart. J. Roy. Meteor. Soc.*, **95,** 544–560.

Best, A. C., 1950: Empirical formulae for the terminal velocity of water drops falling through the atmosphere. *Quart. J. Roy. Meteor. Soc.*, **76,** 302–311.

Braham, R. R., 1952: The water and energy budgets of the thunderstorms and their relation to thunderstorm development. *J. Meteor.*, **9,** 227–242.

Brown, J. M., 1979: Mesoscale unsaturated downdrafts driven by rainfall evaporation: A numerical study. *J. Atmos. Sci.*, **36,** 313–338.

Carbone, R. E., 1982: A severe frontal rainband. Part I: Stormwide hydrodynamic structure. *J. Atmos. Sci.*, **39,** 258–279.

Findeisen, W., 1940: The formation of the 0°C isothermal layer and fractocumulus under nimbostratus. *Meteorol. Z.*, **57,** 49–54.

Geisler, J. E., and F. P. Bretherton, 1969: The sea-breeze forerunner. *J. Atmos. Sci.*, **46,** 82–95.

Harrold, T. W., and K. A. Browning, 1967: Mesoscale wind fluctuations below 1500 meters. *Meteor. Mag.*, **96,** 367–376.

Heymsfield, G. M., 1979: Doppler radar study of a warm frontal region. *J. Atmos. Sci.*, **36,** 2093–2107.

Knight, C. A., 1979: Observations of the morphology of melting snow. *J. Atmos. Sci.*, **36,** 1123–1130.

Leary, C. A., and R. A. Houze, Jr., 1979: Melting and evaporation of hydrometeors in precipitation from anvil clouds of deep tropical convection. *J. Atmos. Sci.*, **36,** 669–679.

Lin, C. A., and R. E. Stewart, 1986: Mesoscale circulations initiated by melting snow. *J. Geophys. Res.*, **91,** 13299–13302.

Marwitz, J. D., 1983: The kinematics of orographic airflow during Sierra storms. *J. Atmos. Sci.*, **40,** 1218–1227.

Matsuo, T., and Y. Sasyo, 1981a: Melting of snowflakes below freezing level in the atmosphere. *J. Meteor. Soc. Japan.*, **59**(1), 10–24.

——, and ——, 1981b: Nonmelting phenomena of snowflakes observed in subsaturated air below freezing level. *J. Meteor. Soc. Japan.*, **59**(1), 26–32.

Ogura, Y., and N. A. Phillips, 1962: Scale analysis of deep and shallow convection in the atmosphere. *J. Atmos. Sci.*, **19,** 173–179.

Orlanski, I., 1976: A simple boundary condition for unbounded hyperbolic flows. *J. Comput. Phys.*, **21,** 251–269.

——, and B. B. Ross, 1973: Numerical simulation of the generation and breaking of internal gravity waves. *J. Geophys. Res.*, **78,** 8808–8826.

——, and ——, 1977: The circulation associated with a cold front. Part I: Dry case. *J. Atmos. Sci.*, **33,** 1619–1633.

Pace, J. C., 1980: Microphysical and thermodynamical characteristics through the melting layer. M.S. thesis, University of Wyoming, AS126, 204 pp.

Stewart, R. E., 1984: Deep 0°C isothermal layers within precipitation bands over southern Ontario. *J. Geophys. Res.*, **89**(D2), 2567–2572.

——, 1985: Precipitation types in winter storms. *Pure Appl. Geophys.*, **123,** 597–609.

——, and P. King, 1987: Rain/snow boundaries over southern Ontario. *Mon. Wea. Rev.*, **115,** 1894–1907.

——, J. D. Marwitz, J. C. Pace and R. E. Carbone, 1984: Characteristics through the melting layer of stratiform cloud. *J. Atmos. Sci.*, **41,** 3227–3237.

Szeto, K. K., 1986: Mesoscale circulations forced by the melting of snow in the atmosphere. M.S. thesis, Department of Physics, University of Toronto, 125 pp.

——, R. E. Stewart and C. A. Lin, 1988: Mesoscale circulations forced by melting snow. Part II: Application to meteorological features. *J. Atmos. Sci.*, **45,** 1642–1650.

Thorpe, A. J., M. J. Miller and M. W. Moncrieff, 1980: Dynamical models of two-dimensional downdrafts. *Quart. J. Roy. Meteor. Soc.*, **106,** 463–484.